



Electronic mechanism for nanoscale skyrmions and topological metalsDeepak S. Kathyat , Arnob Mukherjee , and Sanjeev Kumar *Department of Physical Sciences, Indian Institute of Science Education and Research Mohali,**Sector 81, S.A.S. Nagar, Manauli PO 140306, India*

(Received 22 July 2020; revised 26 November 2020; accepted 9 December 2020; published 8 January 2021)

We report a microscopic electronic mechanism for nanoscale skyrmion formation and topological metallicity originating from Rashba and double-exchange physics. The results are based on hybrid simulations in a model that explicitly retains itinerant electronic degrees of freedom. A simple physical picture is provided via an effective short-range spin model. We identify hexagonal and square lattice arrangements of skyrmions in two different regimes of the parameter space. Sparse skyrmions emerge at finite temperatures as excitations of the ferromagnetic phase. The skyrmion states are characterized as topological metals via explicit calculations of the Bott index and the Hall conductivity. Oscillations in local density of states are shown to arise from a combination of confinement effects and emergent gauge-fields. We also emphasize the importance of a consistent treatment of spin-orbit coupling for calculating electronic properties of metals hosting unconventional magnetic textures such as skyrmions.

DOI: [10.1103/PhysRevB.103.035111](https://doi.org/10.1103/PhysRevB.103.035111)**I. INTRODUCTION**

Magnetic skyrmions are being envisioned as building blocks of next-generation data storage and processing devices [1–6]. This has led to a surge in research activity geared towards identifying candidate materials [7–19]. Such textures in metals are particularly important since they can be manipulated by ultralow electrical currents [10,11,20,21]. The appearance of skyrmions has been reported in bulk as well as in thin films of a variety of chiral metallic magnets [12–15,22–27]. However, the current understanding of skyrmion formation in magnets is via spin Hamiltonians that either include Dzyaloshinskii-Moriya (DM) interactions or geometrical frustration [28–32]. Such studies have also shown the formation of three-dimensional lattices of skyrmions, relevant for skyrmions in bulk [33,34]. This approach is inconsistent for metals as the aforementioned terms are usually understood as arising from the effect of spin-orbit coupling in Mott insulators [35]. Therefore, the importance of electronic Hamiltonian-based understanding of skyrmion formation in metals has been recognized and a mechanism based on Ruderman-Kittel-Kasuya-Yosida interactions has recently been put forward [36,37]. Furthermore, most theoretical studies describe states that are periodic arrangements of skyrmions, whereas experiments on certain thin films or on constricted samples also support a phase with sparse skyrmions [9,27,38,39].

The introduction of the double-exchange (DE) mechanism by Zenger represents a milestone in our understanding of ferromagnetic metals [40–42]. The mechanism has played a key role in the description of magnetic and magneto-transport phenomena across families of materials, such as perovskite manganites, dilute magnetic semiconductors, and Heusler metals [43–46]. Surprisingly, the role of DE physics in skyrmion formation has largely remained unexplored. On the other hand, the DE mechanism is commonly invoked when

studying the effect of magnetic textures, including skyrmions, on transport properties in metals. The implication of spin-orbit-modified DE physics on transport properties has recently been discussed [47].

In this work, we show that the Rashba DE (RDE) model in the presence of Zeeman field leads to states hosting nanoskyrmions. We explicitly demonstrate the appearance of skyrmions using the state-of-the-art hybrid Monte Carlo (HMC) simulations. An effective spin Hamiltonian is studied for a comprehensive understanding of the origin as well as the stability of these spin textures. A filamentary domain wall (fdW) phase is identified as the parent of sparse skyrmions (sSk), which are found to be stable only at finite temperatures and metastable in the ground state, and a single-Q (SQ) spiral state leads to packed skyrmions (pSk). Our findings are consistent with small-angle neutron scattering (SANS) and Lorentz transmission electron microscopy (LTEM) data on thin films of Co-Zn-Mn alloys, FeGe, MnSi, and transition metal multilayers [10–13,18,26,27,48,49]. Furthermore, we explicitly demonstrate by calculating the Bott index and the topological Hall conductivity that the skyrmion phases are a natural realization of amorphous topological metals. This is particularly important in view of recent attempts to engineer tight-binding models for the realization of amorphous topological phases [50–52]. We also present local density of states (LDOS) calculations to show the importance of consistent treatment of spin-orbit coupling for the skyrmion formation and for electronic transport aspects. A combination of dI/dV measurements and LDOS analysis can be a useful alternate to the existing methods for estimating the strength of Rashba coupling in real materials [53].

II. SKYRMIONS IN THE RDE MODEL

We start with the ferromagnetic Kondo lattice model (FKLM) in the presence of Rashba SOC, described by the

following Hamiltonian:

$$H = -t \sum_{\langle ij \rangle, \sigma} (c_{i\sigma}^\dagger c_{j\sigma} + \text{H.c.}) + \lambda \sum_i [(c_{i\downarrow}^\dagger c_{i+x\uparrow} - c_{i\uparrow}^\dagger c_{i+x\downarrow}) + i(c_{i\downarrow}^\dagger c_{i+y\uparrow} + c_{i\uparrow}^\dagger c_{i+y\downarrow}) + \text{H.c.}] - J_H \sum_i \mathbf{S}_i \cdot \mathbf{s}_i. \quad (1)$$

Here, $c_{i\sigma}$ ($c_{i\sigma}^\dagger$) annihilates (creates) an electron at site i with spin σ , and $\langle ij \rangle$ implies that i and j are nearest-neighbor (nn) sites. λ and J_H denote the strengths of Rashba and Hund's coupling, respectively. \mathbf{s}_i is the electronic spin operator at site i , and \mathbf{S}_i , with $|\mathbf{S}_i| = 1$, denotes the localized spin at that site. We parametrize $t = (1 - \alpha)t_0$ and $\lambda = \alpha t_0$ and set $t_0 = 1$ as the reference energy scale. Assuming large J_H and tak-

ing the double-exchange approximation, we obtain the RDE Hamiltonian [54],

$$H_{\text{RDE}} = \sum_{\langle ij \rangle, \gamma} [g_{ij}^\gamma d_i^\dagger d_j + \text{H.c.}] - h_z \sum_i S_i^z, \quad (2)$$

where d_i (d_i^\dagger) annihilates (creates) an electron at site i with spin parallel to the localized spin. The second term represents the Zeeman coupling of local moments to external magnetic field of strength h_z . Site $j = i + \gamma$ is the nn of site i along the spatial direction $\gamma = x$ and y . The projected hopping $g_{ij}^\gamma = t_{ij}^\gamma + \lambda_{ij}^\gamma$ depends on the orientations of the local moments \mathbf{S}_i and \mathbf{S}_j [54]:

$$\begin{aligned} t_{ij}^\gamma &= -t \left[\cos\left(\frac{\theta_i}{2}\right) \cos\left(\frac{\theta_j}{2}\right) + \sin\left(\frac{\theta_i}{2}\right) \sin\left(\frac{\theta_j}{2}\right) e^{-i(\phi_i - \phi_j)} \right], \\ \lambda_{ij}^x &= \lambda \left[\sin\left(\frac{\theta_i}{2}\right) \cos\left(\frac{\theta_j}{2}\right) e^{-i\phi_i} - \cos\left(\frac{\theta_i}{2}\right) \sin\left(\frac{\theta_j}{2}\right) e^{i\phi_j} \right], \\ \lambda_{ij}^y &= i\lambda \left[\sin\left(\frac{\theta_i}{2}\right) \cos\left(\frac{\theta_j}{2}\right) e^{-i\phi_i} + \cos\left(\frac{\theta_i}{2}\right) \sin\left(\frac{\theta_j}{2}\right) e^{i\phi_j} \right], \end{aligned} \quad (3)$$

where θ_i (ϕ_i) denotes the polar (azimuthal) angle for the localized spin \mathbf{S}_i .

We study the RDE Hamiltonian using numerically exact HMC simulations [55] (see also Refs. [56,57] and references therein). The presence of skyrmions is inferred via the local skyrmion density [29],

$$\chi_i = \frac{1}{8\pi} [\mathbf{S}_i \cdot (\mathbf{S}_{i+x} \times \mathbf{S}_{i+y}) + \mathbf{S}_i \cdot (\mathbf{S}_{i-x} \times \mathbf{S}_{i-y})]. \quad (4)$$

The total skyrmion density is defined as $\chi = \sum_i \chi_i$. We also compute the spin structure factor (SSF) as

$$S_f(\mathbf{q}) = \frac{1}{N^2} \sum_{ij} \mathbf{S}_i \cdot \mathbf{S}_j e^{-i\mathbf{q} \cdot (\mathbf{r}_i - \mathbf{r}_j)}, \quad (5)$$

and we compute the relevant component of the vector chirality η as

$$\eta = \frac{1}{N} \sum_i (\mathbf{S}_i \times \mathbf{S}_{i+x}) \cdot \hat{y} - (\mathbf{S}_i \times \mathbf{S}_{i+y}) \cdot \hat{x}. \quad (6)$$

The averaging of all quantities over MC steps is implicitly assumed, unless stated otherwise.

Results obtained via HMC simulations for two representative values of α are shown in Fig. 1. Upon increasing h_z , the magnetization, $M_z = \frac{1}{N} \sum_i S_i^z$, increases and η decreases. The magnitude of χ initially increases with the applied field and then decreases on the approach to the saturated ferromagnetic (sFM) state [see circles in Figs. 1(a) and 1(d)]. The qualitative behavior appears to be similar between $\alpha = 0.25$ and $\alpha = 0.45$. The negative sign of χ reveals that the polarity of skyrmions is opposite to the orientation of the background magnetization.

The existence of skyrmions in the RDE Hamiltonian is explicitly demonstrated via the spin configurations as well as skyrmion density maps in the ground state. We find that small

values of α lead to sparse skyrmions within the zero-field-cooled (ZFC) protocol [see Fig. 1(b)] and the packing (size) of skyrmions increases (decreases) with increasing α [see Fig. 1(e)]. The negative polarity is consistent with the fact that the central spin in the skyrmion texture is oriented opposite to the magnetization direction [see Figs. 1(c) and 1(f)]. We also note that the skyrmions obtained here are of the Neel type with negative effective magnetic monopole charge. In order to understand the origin and stability of sSk and pSk, we present the results of an effective spin model derived from the RDE Hamiltonian.

III. ORIGIN AND STABILITY OF SPARSE AND PACKED SKYRMIONS

Including the Zeeman coupling term in the recently derived effective spin model for H_{RDE} [54], we obtain

$$\begin{aligned} H_{\text{eff}} &= - \sum_{\langle ij \rangle, \gamma} D_{ij}^\gamma f_{ij}^\gamma - h_z \sum_i S_i^z, \\ \sqrt{2} f_{ij}^\gamma &= \{t^2(1 + \mathbf{S}_i \cdot \mathbf{S}_j) + 2t\lambda \hat{\gamma}' \cdot (\mathbf{S}_i \times \mathbf{S}_j) \\ &\quad + \lambda^2[1 - \mathbf{S}_i \cdot \mathbf{S}_j + 2(\hat{\gamma}' \cdot \mathbf{S}_i)(\hat{\gamma}' \cdot \mathbf{S}_j)]\}^{1/2}, \\ D_{ij}^\gamma &= \langle [e^{ih_{ij}^\gamma} d_i^\dagger d_j + \text{H.c.}] \rangle_{\text{gs}}. \end{aligned} \quad (7)$$

In the above, $\hat{\gamma}' = \hat{z} \times \hat{\gamma}$, f_{ij}^γ (h_{ij}^γ) is the modulus (argument) of the complex number g_{ij}^γ , and $\langle \hat{O} \rangle_{\text{gs}}$ denotes expectation values of operator \hat{O} in the ground state. It has been shown that using a constant value of D_{ij}^γ captures the essential physics of the Hamiltonian Eq. (7); therefore, we set $D_{ij}^\gamma \equiv D_0 = 1$ in our simulations [54]. Note that a derivation starting with a simple two-site picture also leads to an identical functional form for the effective spin model [58].

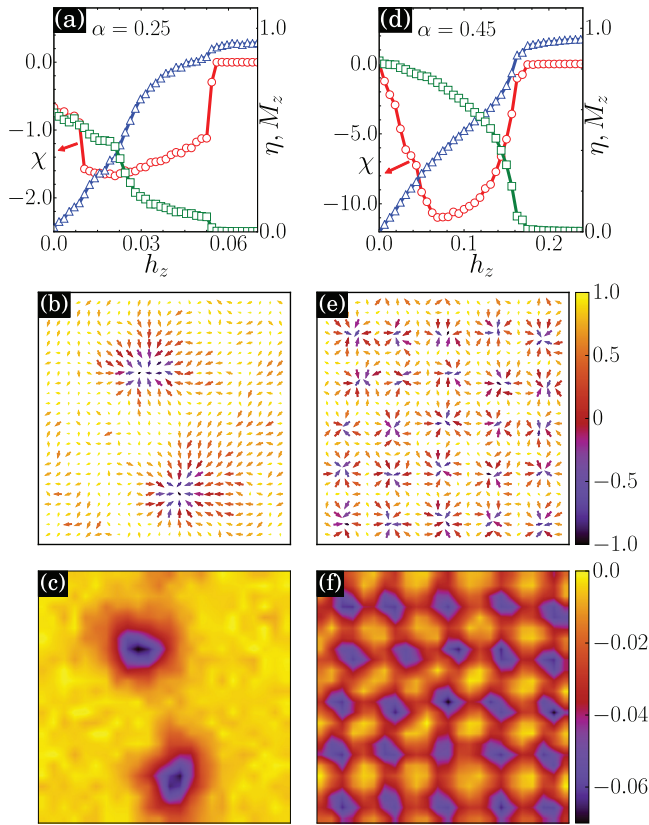


FIG. 1. Magnetization M_z (triangles), total skyrmion density χ (circles), and vector chirality η (squares) as a function of the applied Zeeman field for (a) $\alpha = 0.25$ and (d) $\alpha = 0.45$. Snapshots of spin configurations [panels (b) and (e)] and the local skyrmion density [panels (c) and (f)] at $T = 0.01$ for representative values of α and h_z : (b) and (c) $\alpha = 0.25$ and $h_z = 0.03$; (e) and (f) $\alpha = 0.45$ and $h_z = 0.09$.

We simulate H_{eff} using the conventional classical MC scheme [55]. We find that the field dependence of magnetization, η and χ for H_{eff} , is similar to that obtained via HMC [compare Figs. 1(a) and 1(d) and Fig. 2]. For small values of α , the magnetization increases linearly for small h_z , followed by a slower than linear rise. This change to nonlinear behavior is accompanied by a sharp increase in the magnitude of χ [see Figs. 2(a) and 2(b)]. A simple understanding is that the emergence of skyrmions arrests the ease with which spins align along the direction of the external magnetic field. A finite value of η in the absence of a magnetic field originates from the DM-like terms present in the effective Hamiltonian. The variation of η is anticorrelated with that of magnetization and the former shows a sharp decrease accompanying the increase in magnitude of χ [see Figs. 2(a) and 2(b)]. Finally, for still larger values of the applied field, the system approaches the sFM state, with both χ and η vanishing. For $\alpha = 0.5$, the change in χ near $h_z = 0.25$ is sharper and is accompanied by a weak discontinuity in both magnetization and η [see Fig. 2(c)]. This qualitatively different behavior is an indicator of the pSk state, as is illustrated below with the help of real-space spin configurations. For $\alpha = 0.6$, χ is finite even at $h_z = 0$. This is consistent with our results reported for Rashba FKLm [54]. Interestingly, the magnitude of χ

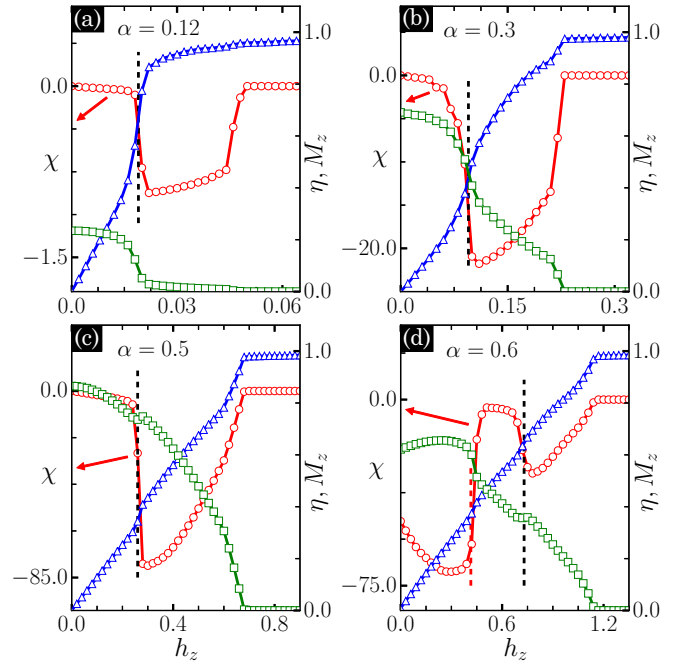


FIG. 2. (a)–(d) Magnetization (triangles), total skyrmion density (circles), and vector chirality (squares) as a function of h_z for different values of α . The left y-axis scale is for χ .

reduces with increasing h_z and then again increases before finally vanishing on approach to the sFM state [see Fig. 2(d)]. The re-entrant behavior of χ shows that the skyrmion crystal (SkX) state does not directly lead to the sFM state via isolated skyrmions, instead a SQ spiral phase is stabilized at intermediate h_z before the sFM state appears in the strong field limit. This suggests that in contrast to the pSk phase, which can be viewed as a packed arrangement of isolated skyrmions, the SkX phase should be interpreted as a fully cooperative ordered arrangement of spins stable only in the low-field regime. Note that square lattice of skyrmions has also been reported in experiments [59,60]

We find that, within the ZFC protocol at finite temperatures, the domain junctions in the fdW states for small α [see Fig. 3(a)] become nucleation centers for skyrmions when a magnetic field is applied [see Fig. 3(b)]. For larger values of α , the SQ spiral state gives way to the pSk phase [see Fig. 3(c)]. For a given α , increasing h_z leads, initially, to a reduction of the size [compare Figs. 3(c) and 3(d)] and then to a reduction of the number of skyrmions [55]. We have also confirmed that the skyrmion formation in the model is not an artifact of the ZFC protocol by verifying their existence using the field-cooled protocol [55]. However, an important question is whether the sSk phase is a thermodynamically stable ground state phase. By comparing energies between increasing- and decreasing- h_z simulations at low temperatures we find that a saturated ferromagnet has lower energy compared to that of the sSk phase. Therefore, the sSk phase is not a stable ground state phase. We perform additional simulations starting at low temperatures with a sFM configuration and find that isolated skyrmions spontaneously form by simply increasing the temperature in simulations (see Fig. 4). This suggests that the sSk phase is entropically favored over the sFM phase and

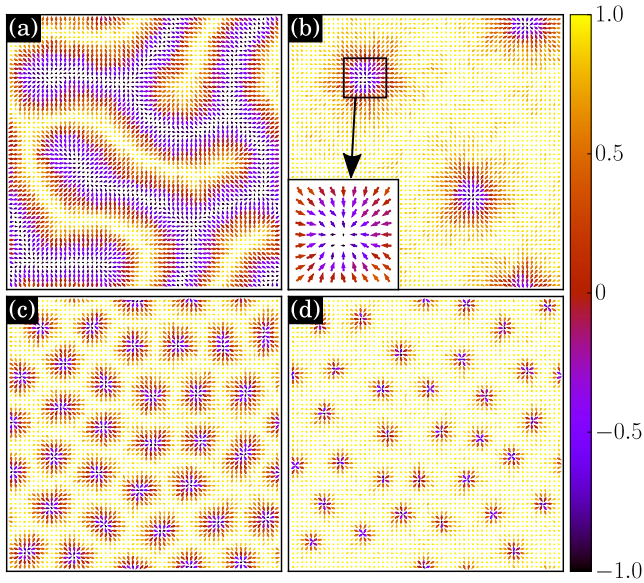


FIG. 3. Low-temperature snapshots of spin configurations for representative values of α and h_z . (a) fDW state at $\alpha = 0.16$ and $h_z = 0$, (b) sparse skyrmions at $\alpha = 0.16$ and $h_z = 0.036$, (c) pSk at $\alpha = 0.32$ and $h_z = 0.13$, and (d) pSk at $\alpha = 0.32$ and $h_z = 0.21$.

hence it should be relevant to real systems. We show how the skyrmion count n_{Sk} first increases and then decreases upon increasing T [see inset in Fig. 4(b)]. A possible interpretation is that isolated skyrmions exist as thermal excitations in the ferromagnetic background. However, a confirmation of this requires more systematic exploration of the model at finite temperatures which will be taken up in a separate study. The reduction of n_{Sk} with increasing temperature correlates with the transition of the parent ferromagnetic state into a paramagnetic state.

We now summarize the results discussed above in the form of a phase diagram in Fig. 5(a). We identify, in addition to the trivial sFM state, (i) a fDW state, (ii) a SQ spiral with peaks in the spin structure factor at $(0, Q)$ or $(Q, 0)$, (iii) a pSk state, and (iv) a SkX with square geometry. Furthermore, a metastable sSk region is also indicated in the ground state phase diagram. The boundary between fDW/SQ and sSk/pSk is determined from the sharp increase in the magnitude of χ with increasing h_z [see dashed black lines in Figs. 2(a)–2(d)]. Similarly, the boundary between SkX and SQ is inferred from the variation in χ [see dashed red line in Fig. 2(d)]. Note that the sharp change in χ is accompanied by a weak but noticeable change in h_z dependence in magnetization and chirality. The sFM boundary is defined by the saturation of magnetization together with a complete vanishing of chirality and skyrmion density. It is important to mention that the finite- T sSk phase can only be characterized by real-space images showing the presence of isolated skyrmions. Since these isolated skyrmions exist in the ferromagnetic background any bulk indicators, such as the SSF, will identify this phase as a ferromagnet. Since the definition of the sSk state as a true thermodynamic phase is not possible, we indicate this as a metastable region just below the sFM phase boundary. This is to be understood as the region where isolated skyrmions

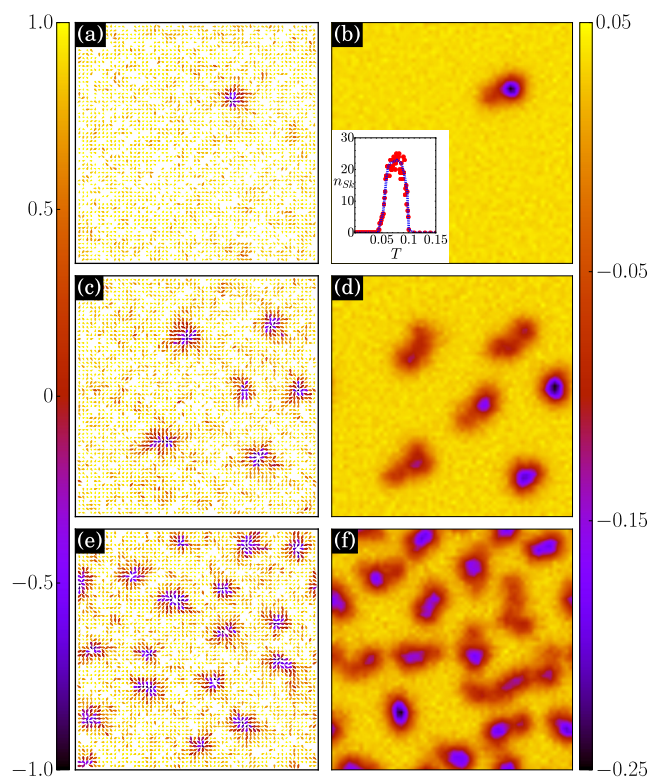


FIG. 4. Snapshots of typical spin configurations (left column) and corresponding skyrmion density map (right column) taken from Monte Carlo simulations with increasing temperature starting from the sFM state at $T = 0.001$. (a) and (b): $T = 0.044$, (c) and (d): $T = 0.052$, and (e) and (f): $T = 0.058$. The inset in panel (b) shows the variation in the skyrmion count n_{Sk} with the temperature confirming the existence of isolated skyrmions in the ferromagnetic background as finite- T excitations. The calculations were performed on a 60×60 lattice at $\alpha = 0.25$ and $h_z = 0.1$.

will emerge at finite temperatures. The boundary between pSk and sSk states is obtained from the h_z dependence of the explicit skyrmion count n_{Sk} . In the pSk phase, the number of skyrmions does not change upon changing the external magnetic field [see the inset in Fig. 5(a)]. Strictly at $T = 0$, the skyrmion count should exhibit a steplike jump to zero. However, at finite T there is a narrow region in h_z displaying a steep decrease in the skyrmion count. A similar gradual decrease in the skyrmion count is expected upon increasing the temperature close to the paramagnetic phase boundary. This can be interpreted as a melting of the skyrmion lattice via the sSk state [61].

The SSF for the fDW, pSk, and SkX states are displayed in Figs. 5(b)–5(d), in that order. The circular diffuse pattern for small α [see Figs. 5(b) and 5(c)] matches well with SANS experiments and Fourier transform of LTEM images on MnSi and Co-Zn-Mn alloys [11,15,18]. We also characterize the pSk state by plotting the number of skyrmions n_{Sk} as a function of the applied field. A plateau in n_{Sk} is an indicator of the pSk state [see the inset in Fig. 5(a)].

The SSF in the pSk phase seems to have a hexagonal symmetry. This is expected as close packing of disk-shaped particles will naturally lead to the formation of a triangular

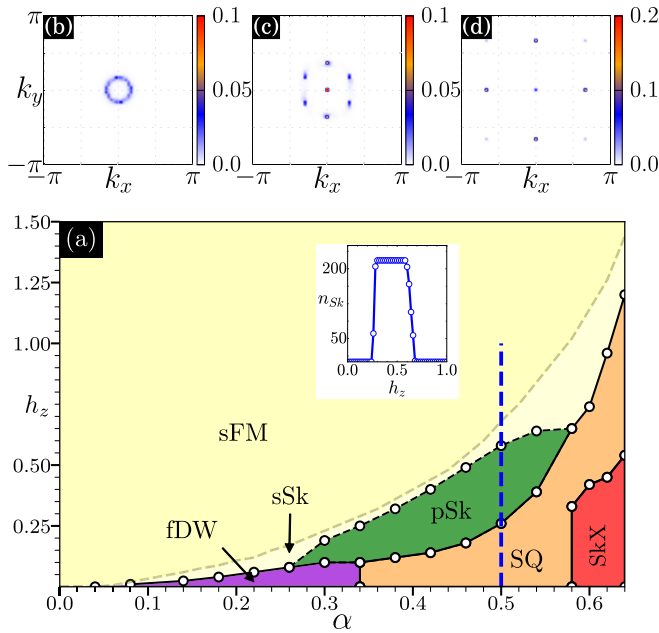


FIG. 5. (a) Low-temperature phase diagram in the α - h_z plane. SSFs for (b) fDW at $\alpha = 0.22$ and $h_z = 0$, (c) pSk at $\alpha = 0.4$ and $h_z = 0.16$, and (d) SkX at $\alpha = 0.6$ and $h_z = 0.3$. The inset in panel (a) shows an explicit count of the skyrmion centers n_{sk} as a function of h_z along the vertical dashed line at $\alpha = 0.5$. The sSk phase is metastable and the sFM state is the true ground state in that parameter regime.

lattice. However, on a closer look one finds that the points on the k_y axis are more intense than those located close to the diagonals. We have identified the origin of this asymmetry in the SSF of the $h_z = 0$ state. As mentioned earlier, the spirals in the $h_z = 0$ SQ phase are doubly degenerate with the $(0, Q)$ and $(Q, 0)$ spirals having identical energies. In simulations, one of these spirals is spontaneously stabilized at low temperatures. By selecting two such simulations where different SQ states were stabilized, and by increasing h_z in the ZFC protocol, we obtain pSk phases characterized by an SSF pattern that has a relative 90° rotation [compare Figs. 6(b) and 6(d)]. In either case, the peaks located on the k_x or k_y axis are relatively intense. Observation of these asymmetries suggest that formation of an emergent lattice of extended particles residing on, and defined from, the sites of a square lattice cannot form a perfect hexagonal structure. Clearly, in continuum a triangular lattice can spontaneously form with arbitrary orientations of the three defining axes. On a square lattice, however, the x or y direction becomes a natural choice for one of the axes of the triangular lattice, leading to a stronger intensity in the SSF along that direction.

In Sec. II, we have shown that the RDE model can account for the formation of skyrmions within an electronic Hamiltonian without the need to write a spin-only model. In Sec. III, we explicitly verified that the connection of the electronic Hamiltonian approach to the standard DM-interaction-based approach to skyrmion formation is understood via the effective spin Hamiltonian derived in our earlier work [54]. While it is well known that itinerant electrons strongly coupled to a magnetic skyrmion background generate an

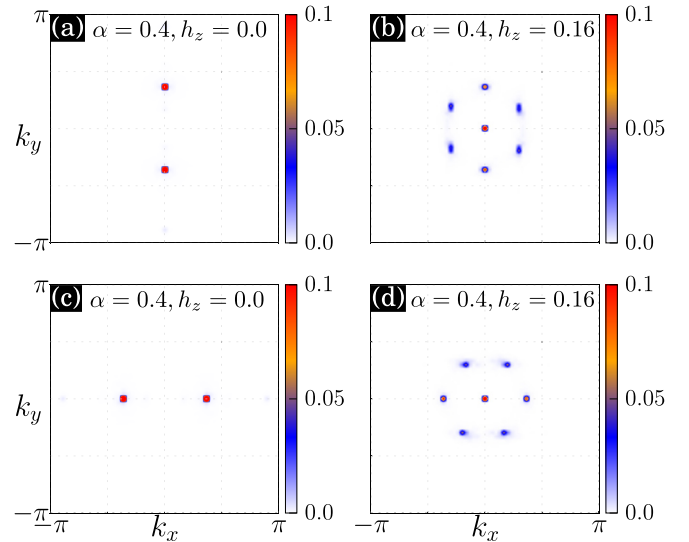


FIG. 6. SSF for $h_z = 0$ [panels (a) and (c)] and $h_z = 0.16$ [panels (b) and (d)] in two independent simulations. The ground state in the absence of the magnetic field is doubly degenerate with $(0, Q)$ and $(Q, 0)$ spirals having equal energy. The hexagonal pattern in the SSF at a finite magnetic field displaying a slight asymmetry related to the $h_z = 0$ spiral state.

anomalous response in transport [31,62], the influence of Rashba coupling on transport properties has been pointed out only recently [47]. For consistency and completeness, in the next section we discuss the effect of magnetic skyrmion states on the electronic properties. This is important to emphasize as in the existing literature it is common practice to use the standard DE model for studying the response of itinerant electrons to unconventional spin textures [30,62–64]. The fact that spin-orbit interactions play a crucial role in stabilizing skyrmion textures is commonly ignored when analyzing the response of itinerant electrons to skyrmions and the resulting anomalous Hall physics.

IV. BOTT INDEX AND TOPOLOGICAL METALICITY

The possibility of finding amorphous analogs of translationally invariant topological insulators has attracted much attention in recent years. Models for disordered topological metallic or insulating states have been proposed [50,65]. A crucial feature of these models is a spatially dependent pattern of hopping parameters which may not be easy to realize. It is well known that electrons coupled to noncoplanar magnetic patterns experience an effective magnetic field and generate an anomalous Hall effect [31,62]. We study how the presence of Rashba coupling in the DE model affects this anomalous response. We present topological characterization of the sSk and pSk states by computing the Bott index \mathcal{B} and the Hall conductivity σ_{xy} [55] (see also Refs. [51,52] therein). Loring and Hastings first introduced the concept of Bott index in condensed matter systems [66,67]. It is a measure of the incapability of the system to form localized Wannier orbitals from the occupied states [67]. Our motivation to compute the Bott index here is to mathematically confirm the topological aspect of the band structure of electrons in the presence of magnetic

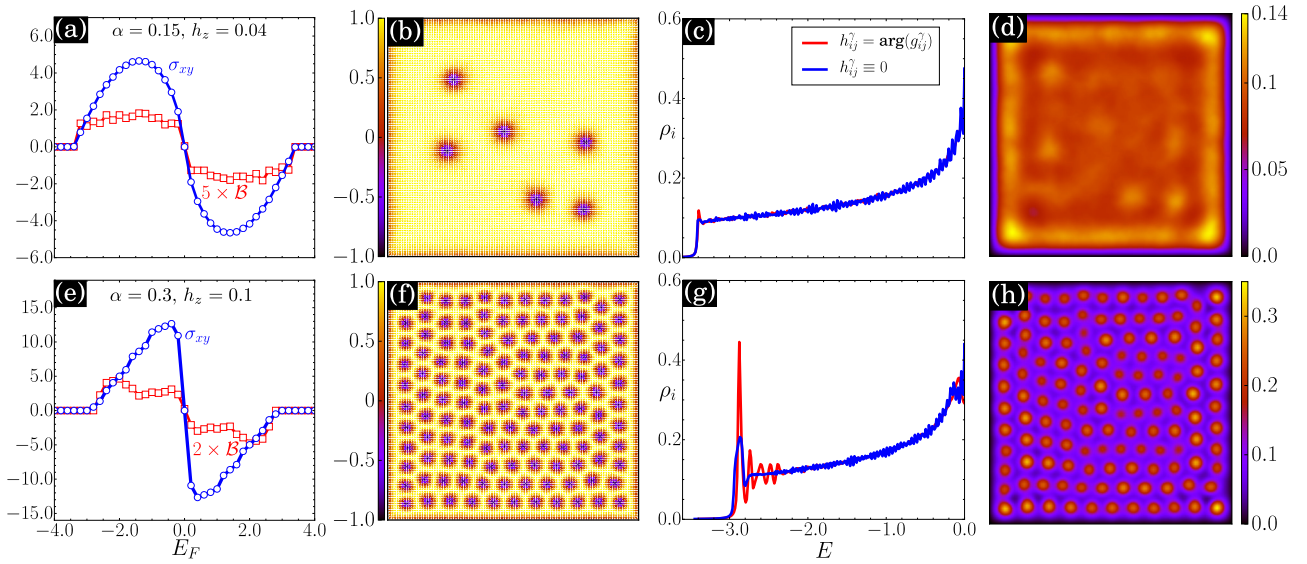


FIG. 7. (a) Bott index \mathcal{B} and Hall conductivity σ_{xy} (in units of e^2/h) as functions of the Fermi level E_F , (b) low-temperature magnetic configuration obtained via simulations with open boundary conditions, (c) LDOS at skyrmion cores with (red lines) and without (blue lines) local gauge fields, and (d) real-space map of LDOS at $E = -3.38$ in the absence of local gauge fields ($h_{ij}^\gamma \equiv 0$). Panels (a)–(d) display results for $\alpha = 0.15$. Panels (e)–(h) show the same quantities as shown in panels (a)–(d), in that order, for $\alpha = 0.30$. LDOS in panel (h) is shown for $E = -2.87$. The results are obtained on 100×100 lattice using open boundary conditions.

skyrmion states. The implementation details of the Bott index calculation can be found in the literature [50–52,68]. Nevertheless, for completeness we outline the key steps below. The first step is to construct a projection operator out of all the occupied states:

$$P = \sum_{k=1}^{Nel} |\psi_k\rangle\langle\psi_k|, \quad (8)$$

where $|\psi_k\rangle$ is the occupied eigenstate corresponding to the k th eigenvalue E_k , and Nel is the number of electrons in the system. The position coordinates (x_i, y_i) of any lattice site i can be mapped into the spherical coordinates (Θ_i, Φ_i) on a torus where $0 \leq \Theta_i < 2\pi$ and $0 \leq \Phi_i < 2\pi$. The next step is to define the projected position operators,

$$U = Pe^{i\Theta}P, \quad V = Pe^{i\Phi}P, \quad (9)$$

where Θ and Φ are the diagonal matrices with Θ_i and Φ_i as diagonal elements, respectively. The Bott index is given by

$$B = \frac{1}{2\pi} \text{Im}\{\text{tr}[\log(VUV^\dagger U^\dagger)]\}, \quad (10)$$

For numerical stability of the algorithm, we perform singular value decomposition of the projected position operators U and V following Huang and Liu [51,52]. The Hall conductivity σ_{xy} is computed using the Kubo formula [55]. Both sSk and pSk states support finite values of σ_{xy} as well as \mathcal{B} [see Figs. 7(a) and 7(e)]. Both quantities display a change of sign as the Fermi level crosses zero. Since the Bott index is an analog of the Chern index for inhomogeneous systems, the aforementioned correspondence between the Hall conductivity and the Bott index confirms the topological aspect of the skyrmion phases in the RDE model in the same manner as the finite Chern index confirms the topological nature of states in translationally invariant systems. Therefore, metallic systems

with few or many skyrmions can be classified as topological metals in close analogy with recently proposed hopping-pattern-engineered tight-binding models [50,65]. Further, the larger magnitude of σ_{xy} in Fig. 7(e) compared to that in Fig. 7(a) is due to the increase in the number of skyrmions. In the sparse skyrmion regime, the Hall conductivity increases linearly with the number of skyrmions. The dependence becomes sublinear on approach to a pSk phase. On the other hand, in the pSk phase increasing the number of skyrmions necessarily leads to a decrease in the size of skyrmions. The consequence is larger gauge fields and hence a smaller and quantized Hall conductivity (see Fig. S1 in the Supplemental Material [55]).

In order to further differentiate between the Rashba-modified DE mechanism from the standard DE physics, we calculate the LDOS, $\rho_i(E) = 1/N \sum_k |\psi_i^k|^2 \delta(E - E_k)$, where ψ_i^k is the amplitude on site i of the single-particle eigenstate $|\psi_k\rangle$ corresponding to eigenvalue E_k of the RDE Hamiltonian Eq. (2). A Lorentzian with broadening parameter 0.01 is used to approximate the Dirac delta function. We find that the skyrmion textures in magnetization have strong implications for the electronic wave functions in this unusual metallic phase. We use open boundary conditions for LDOS calculations in order to illustrate the presence of edge modes due to skyrmion-induced gauge fields [55]. Note that the open boundary condition results lead to visible textures in magnetization along the edges. These are a simple consequence of competition between DM-like and ferromagnetic terms in the spin Hamiltonian along the edges and are unrelated to the presence of skyrmions in the bulk. We focus on the LDOS for sites located in skyrmion cores. In the sparse skyrmion case, there is a weak enhancement in LDOS near the band edge [see Fig. 7(c)]. The effect becomes much pronounced for the packed skyrmion state. Furthermore, periodic modulations as a function of energy become clear [see Fig. 7(g)].

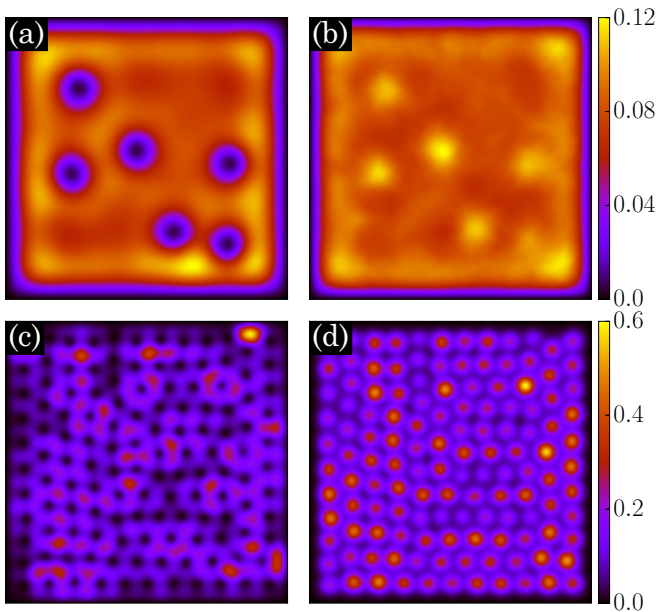


FIG. 8. For the sSk configuration obtained at $\alpha = 0.15$ and $h_z = 0.04$ [shown in Fig. 7(b)]: LDOS map for energy near the band edge (a) in an inconsistent electronic model with $\alpha = 0.0$ and (b) for the consistent calculation with $\alpha = 0.15$ in the itinerant model. For the pSk configuration shown in Fig. 7(f): LDOS maps within (c) the inconsistent calculation with $\alpha = 0.0$ and (d) the consistent calculation with $\alpha = 0.30$. Note the qualitative difference between the left and right columns: while the skyrmion cores behave as repulsive centers for electrons in $\alpha = 0$ calculations, they become attractive centers in the consistent calculations.

The inset in Fig. 7(g) shows the energy difference of two consecutive peaks, ΔE_n , as a function of peak index. There are two possible interpretations of the spikes in LDOS. They can appear either due to the confinement effect, similar to those reported in metallic nanoislands and carbon nanotubes with defect [69,70] or due to effective magnetic flux hidden in the gauge fields. We find a clear approach to disentangle these two effects. Ignoring the phases in the complex hopping parameters g_{ij}^y in the RDE Hamiltonian sets the gauge fields to zero, and the resulting model with real hopping parameters contains pure confinement effects. The results of LDOS calculations using $h_{ij}^y \equiv 0$ in Eq. (2) [blue lines in Figs. 7(c) and 7(g)] show that the periodic modulations vanish and only a single peak near the band edge survives. In Figs. 7(d) and 7(h), we plot lattice maps of LDOS for the energy fixed at peak locations. The resulting maps display inhomogeneities and a clear localization of electronic wave functions at skyrmion cores for the pSk state [see Fig. 7(h)]. Note that the depletion of LDOS along the edges visible in Fig. 7(d) is related to the magnetic texture along the edges in Fig. 7(b) and is not a topological feature. The above analysis proves that, although the confinement effects are present due to changes in the magnitude of g_{ij}^y , the oscillations can only be explained by Landau level physics arising from effective magnetic flux hidden in complex g_{ij}^y . This is further confirmed by performing LDOS calculations on ideal skyrmion lattices where we explicitly show quantization of σ_{xy} [55] (see also Ref. [71] and references therein).

In order to clearly emphasize the importance of a consistent treatment of Rashba coupling in the DE mechanism of skyrmion formation, we demonstrate the qualitative difference between LDOS maps obtained without and with the Rashba term. Once again we take the typical configurations from sSk and pSk phases for this demonstration. For both sSk and pSk states, LDOS maps calculated by setting $\alpha = 0$ display a depletion of electron density near skyrmion cores [see Figs. 8(a) and 8(c)]. When the consistent calculations are performed by setting the value of α equal to that used for obtaining the skyrmion textures, an opposite qualitative picture emerges. The skyrmion cores tend to behave as attraction centers for the electronic charge [see Figs. 8(b) and 8(d)]. This change of qualitative behavior is a clear sign of caution for the calculations performed within the conventional DE approach.

V. CONCLUSION

The double-exchange mechanism provides a basis for understanding ferromagnetism in a variety of metallic magnets. We have uncovered an aspect associated with the classic DE mechanism by including the effect of Rashba SOC and the Zeeman field in the DE model. An explicit demonstration of the existence of nanoscale skyrmions in an electronic model with no direct spin-spin interactions is presented. In the presence of a magnetic field, at finite temperatures, phases with sparse as well as packed skyrmions are stabilized. While the pSk states are shown to be true ground states of the model, the sparse skyrmions are metastable in the ground state but occur at finite temperature as excitations of the ferromagnet. The circular patterns in the SSF are remarkably similar to those reported in the SANS experiments on Co-Zn-Mn alloys and MnSi [15,18]. The corresponding real-space images, representative of fDW states, are also in agreement with the LTEM images on FeGe, Co-Zn-Mn, and transition metal multilayers [[8–10,12,13,15,27],[48,49]]. The origin of the skyrmion states lies in the anisotropy terms of the DM interaction and the pseudodipolar form that become apparent in the effective Hamiltonian derived from the RDE model. In addition to a hexagonal packed lattice of skyrmions, we also find a qualitatively different square lattice skyrmion crystal stable for larger values of α . Hall conductivity and Bott index calculations are presented to explicitly demonstrate that the skyrmion states are examples of amorphous topological metals. Analogy with recently proposed tight-binding models for amorphous topological metals and insulators is also discussed. The LDOS calculations are presented in order to emphasize the importance of Rashba coupling in the DE mechanism that is commonly used for analyzing the influence of magnetic textures on electronic transport. The characteristic oscillations in LDOS as a function of energy can be directly measured in experiments via dI/dV spectra. Such dI/dV measurements can also be used to estimate the strength of Rashba coupling in a metal with the help of a careful modeling of the data.

ACKNOWLEDGMENTS

We thank Goutam Sheet and Yogesh Singh for valuable discussions. We acknowledge the use of the computing facility at IISER Mohali.

- [1] A. Fert, N. Reyren, and V. Cros, *Nat. Rev. Mater.* **2**, 17031 (2017).
- [2] R. Wiesendanger, *Nat. Rev. Mater.* **1**, 16044 (2016).
- [3] A. Fert, V. Cros, and J. Sampaio, *Nat. Nanotechnol.* **8**, 152 (2013).
- [4] N. Nagaosa and Y. Tokura, *Nat. Nanotechnol.* **8**, 899 (2013).
- [5] B. Göbel, A. Mook, J. Henk, and I. Mertig, *Phys. Rev. B* **99**, 020405(R) (2019).
- [6] A. N. Bogdanov and C. Panagopoulos, *Phys. Today* **73**(3), 44 (2020).
- [7] B. Dupé, M. Hoffmann, C. Paillard, and S. Heinze, *Nat. Commun.* **5**, 4030 (2014).
- [8] S. D. Pollard, J. A. Garlow, J. Yu, Z. Wang, Y. Zhu, and H. Yang, *Nat. Commun.* **8**, 14761 (2017).
- [9] A. Soumyanarayanan, M. Raju, A. L. Gonzalez Oyarce, A. K. C. Tan, M.-Y. Im, A. Petrović, P. Ho, K. H. Khoo, M. Tran, C. K. Gan, F. Ernult, and C. Panagopoulos, *Nat. Mater.* **16**, 898 (2017).
- [10] N. Romming, C. Hanneken, M. Menzel, J. E. Bickel, B. Wolter, K. von Bergmann, A. Kubetzka, and R. Wiesendanger, *Science* **341**, 636 (2013).
- [11] X. Z. Yu, N. Kanazawa, W. Z. Zhang, T. Nagai, T. Hara, K. Kimoto, Y. Matsui, Y. Onose, and Y. Tokura, *Nat. Commun.* **3**, 988 (2012).
- [12] X. Z. Yu, N. Kanazawa, Y. Onose, K. Kimoto, W. Z. Zhang, S. Ishiwata, Y. Matsui, and Y. Tokura, *Nat. Mater.* **10**, 106 (2011).
- [13] X. Zhao, C. Jin, C. Wang, H. Du, J. Zang, M. Tian, R. Che, and Y. Zhang, *Proc. Natl. Acad. Sci. U.S.A.* **113**, 4918 (2016).
- [14] S. Meyer, M. Perini, S. von Malottki, A. Kubetzka, R. Wiesendanger, K. von Bergmann, and S. Heinze, *Nat. Commun.* **10**, 3823 (2019).
- [15] A. Tonomura, X. Yu, K. Yanagisawa, T. Matsuda, Y. Onose, N. Kanazawa, H. S. Park, and Y. Tokura, *Nano Lett.* **12**, 1673 (2012).
- [16] M. Hirschberger, T. Nakajima, S. Gao, L. Peng, A. Kikkawa, T. Kurumaji, M. Kriener, Y. Yamasaki, H. Sagayama, H. Nakao, K. Ohishi, K. Kakurai, Y. Taguchi, X. Yu, T.-h. Arima, and Y. Tokura, *Nat. Commun.* **10**, 5831 (2019).
- [17] C. Jin, Z.-A. Li, A. Kovács, J. Caron, F. Zheng, F. N. Rybakov, N. S. Kiselev, H. Du, S. Blügel, M. Tian, Y. Zhang, M. Farle, and R. E. Dunin-Borkowski, *Nat. Commun.* **8**, 15569 (2017).
- [18] K. Karube, J. S. White, N. Reynolds, J. L. Gavilano, H. Oike, A. Kikkawa, F. Kagawa, Y. Tokunaga, H. M. Rønnow, Y. Tokura, and Y. Taguchi, *Nat. Mater.* **15**, 1237 (2016).
- [19] S. Mühlbauer, B. Binz, F. Jonietz, C. Pfleiderer, A. Rosch, A. Neubauer, R. Georgii, and P. Böni, *Science* **323**, 915 (2009).
- [20] K. M. Song, J.-S. Jeong, B. Pan, X. Zhang, J. Xia, S. Cha, T.-E. Park, K. Kim, S. Finizio, J. Raabe, J. Chang, Y. Zhou, W. Zhao, W. Kang, H. Ju, and S. Woo, *Nat. Electron.* **3**, 148 (2020).
- [21] J. Sampaio, V. Cros, S. Rohart, A. Thiaville, and A. Fert, *Nat. Nanotechnol.* **8**, 839 (2013).
- [22] A. K. Nayak, V. Kumar, T. Ma, P. Werner, E. Pippel, R. Sahoo, F. Damay, U. K. Röbber, C. Felser, and S. S. P. Parkin, *Nature (London)* **548**, 561 (2017).
- [23] C. Pfleiderer, D. Reznik, L. Pintschovius, H. v. Löhneysen, M. Garst, and A. Rosch, *Nature (London)* **427**, 227 (2004).
- [24] J. Jena, B. Göbel, T. Ma, V. Kumar, R. Saha, I. Mertig, C. Felser, and S. S. P. Parkin, *Nat. Commun.* **11**, 1115 (2020).
- [25] P.-J. Hsu, L. Rózsa, A. Finco, L. Schmidt, K. Palotás, E. Vedmedenko, L. Udvardi, L. Szunyogh, A. Kubetzka, K. von Bergmann, and R. Wiesendanger, *Nat. Commun.* **9**, 1571 (2018).
- [26] X. Z. Yu, W. Koshibae, Y. Tokunaga, K. Shibata, Y. Taguchi, N. Nagaosa, and Y. Tokura, *Nature (London)* **564**, 95 (2018).
- [27] T. Nagase, M. Komatsu, Y. G. So, T. Ishida, H. Yoshida, Y. Kawaguchi, Y. Tanaka, K. Saitoh, N. Ikarashi, M. Kuwahara, and M. Nagao, *Phys. Rev. Lett.* **123**, 137203 (2019).
- [28] U. K. Röbber, A. N. Bogdanov, and C. Pfleiderer, *Nature (London)* **442**, 797 (2006).
- [29] J. P. Chen, D.-W. Zhang, and J. M. Liu, *Sci. Rep.* **6**, 29126 (2016).
- [30] N. Mohanta, E. Dagotto, and S. Okamoto, *Phys. Rev. B* **100**, 064429 (2019).
- [31] J. Zang, M. Mostovoy, J. H. Han, and N. Nagaosa, *Phys. Rev. Lett.* **107**, 136804 (2011).
- [32] J. Iwasaki, A. J. Beekman, and N. Nagaosa, *Phys. Rev. B* **89**, 064412 (2014).
- [33] S. G. Yang, Y. H. Liu, and J. H. Han, *Phys. Rev. B* **94**, 054420 (2016).
- [34] X. X. Zhang, A. S. Mishchenko, G. De Filippis, and N. Nagaosa, *Phys. Rev. B* **94**, 174428 (2016).
- [35] A. Farrell and T. Pereg-Barnea, *Phys. Rev. B* **89**, 035112 (2014).
- [36] R. Ozawa, S. Hayami, and Y. Motome, *Phys. Rev. Lett.* **118**, 147205 (2017).
- [37] Z. Wang, Y. Su, S.-Z. Lin, and C. D. Batista, *Phys. Rev. Lett.* **124**, 207201 (2020).
- [38] W. Jiang, P. Upadhyaya, W. Zhang, G. Yu, M. B. Jungfleisch, F. Y. Fradin, J. E. Pearson, Y. Tserkovnyak, K. L. Wang, O. Heinonen, S. G. Te Velthuis, and A. Hoffmann, *Science* **349**, 283 (2015).
- [39] N. Mathur, M. J. Stolt, and S. Jin, *APL Mater.* **7**, 120703 (2019).
- [40] C. Zener, *Phys. Rev.* **82**, 403 (1951).
- [41] P. W. Anderson and H. Hasegawa, *Phys. Rev.* **100**, 675 (1955).
- [42] P. G. de Gennes, *Phys. Rev.* **118**, 141 (1960).
- [43] E. Dagotto, *Nanoscale Phase Separation and Colossal Magnetoresistance* (Springer, Berlin, 2002).
- [44] K. Pradhan and S. K. Das, *Sci. Rep.* **7**, 9603 (2017).
- [45] A. Yaouanc, P. Dalmas de Réotier, B. Roessli, A. Maisuradze, A. Amato, D. Andreica, and G. Lapertot, *Phys. Rev. Res.* **2**, 013029 (2020).
- [46] D. Bombor, C. G. F. Blum, O. Volkonskiy, S. Rodan, S. Wurmehl, C. Hess, and B. Büchner, *Phys. Rev. Lett.* **110**, 066601 (2013).
- [47] S.-S. Zhang, H. Ishizuka, H. Zhang, G. B. Halász, and C. D. Batista, *Phys. Rev. B* **101**, 024420 (2020).
- [48] K. Karube, J. S. White, D. Morikawa, C. D. Dewhurst, R. Cubitt, A. Kikkawa, X. Yu, Y. Tokunaga, T.-h. Arima, H. M. Rønnow, Y. Tokura, and Y. Taguchi, *Sci. Adv.* **4**, eaar7043 (2018).
- [49] Y. Tokunaga, X. Z. Yu, J. S. White, H. M. Rønnow, D. Morikawa, Y. Taguchi, and Y. Tokura, *Nat. Commun.* **6**, 7638 (2015).
- [50] A. Agarwala and V. B. Shenoy, *Phys. Rev. Lett.* **118**, 236402 (2017).
- [51] H. Huang and F. Liu, *Phys. Rev. Lett.* **121**, 126401 (2018).
- [52] H. Huang and F. Liu, *Phys. Rev. B* **98**, 125130 (2018).
- [53] D. C. Vaz, F. Trier, A. Dyrdał, A. Johansson, K. Garcia, A. Barthélémy, I. Mertig, J. Barnaś, A. Fert, and M. Bibes, *Phys. Rev. Mater.* **4**, 071001(R) (2020).

- [54] D. S. Kathyat, A. Mukherjee, and S. Kumar, *Phys. Rev. B* **102**, 075106 (2020).
- [55] See Supplemental Material at <http://link.aps.org/supplemental/10.1103/PhysRevB.103.035111> for further details.
- [56] S. Kumar and P. Majumdar, *Eur. Phys. J. B* **50**, 571 (2006).
- [57] A. Mukherjee, N. D. Patel, C. Bishop, and E. Dagotto, *Phys. Rev. E* **91**, 063303 (2015).
- [58] S. Banerjee, J. Rowland, O. Erten, and M. Randeria, *Phys. Rev. X* **4**, 031045 (2014).
- [59] N. D. Khanh, T. Nakajima, X. Yu, S. Gao, K. Shibata, M. Hirschberger, Y. Yamasaki, H. Sagayama, H. Nakao, L. Peng, K. Nakajima, R. Takagi, T. hisa Arima, Y. Tokura, and S. Seki, *Nat. Nanotechnol.* **15**, 444 (2020).
- [60] T. Tanigaki, K. Shibata, N. Kanazawa, X. Yu, Y. Onose, H. S. Park, D. Shindo, and Y. Tokura, *Nano Lett.* **15**, 5438 (2015).
- [61] Y. Nishikawa, K. Hukushima, and W. Krauth, *Phys. Rev. B* **99**, 064435 (2019).
- [62] B. Göbel, A. Mook, J. Henk, and I. Mertig, *Eur. Phys. J. B* **91**, 179 (2018).
- [63] K. Hamamoto, M. Ezawa, and N. Nagaosa, *Phys. Rev. B* **92**, 115417 (2015).
- [64] B. Göbel, A. Mook, J. Henk, and I. Mertig, *Phys. Rev. B* **95**, 094413 (2017).
- [65] Y.-B. Yang, T. Qin, D.-L. Deng, L.-M. Duan, and Y. Xu, *Phys. Rev. Lett.* **123**, 076401 (2019).
- [66] T. A. Loring and M. B. Hastings, *Europhys. Lett.* **92**, 67004 (2010).
- [67] M. B. Hastings and T. A. Loring, *Ann. Phys. (New York)* **326**, 1699 (2011).
- [68] D. Toniolo, *Phys. Rev. B* **98**, 235425 (2018).
- [69] H.-T. Yang, J.-W. Chen, L.-F. Yang, and J. Dong, *Phys. Rev. B* **71**, 085402 (2005).
- [70] M. V. Rastei, B. Heinrich, L. Limot, P. A. Ignatiev, V. S. Stepanyuk, P. Bruno, and J. P. Bucher, *Phys. Rev. Lett.* **99**, 246102 (2007).
- [71] F. Tejo, A. Riveros, J. Escrig, K. Y. Guslienko, and O. Chubykalo-Fesenko, *Sci. Rep.* **8**, 6280 (2018).